ACS OMEGA

http://pubs.acs.org/journal/acsodf

Article

Band-Gap Tuning Induced by Germanium Introduction in Solution-Processed Kesterite Thin Films

Giorgio Tseberlidis, Vanira Trifiletti, Elisa Vitiello, Amin Hasan Husien, Luigi Frioni, Mattia Da Lisca, José Alvarez, Maurizio Acciarri, and Simona O. Binetti*

Cite This: *ACS Omega* 2022, 7, 23445−23456

Read Online

ACCESS | Metrics & More | Article Recommendations

ABSTRACT: In the last few decades, the attention of scientific community has been driven toward the research on renewable energies. In particular, the photovoltaic (PV) thin-film technology has been widely explored to provide suitable candidates as top cells for tandem architectures, with the purpose of enhancing current PV efficiencies. One of the most studied absorbers, made of earth-abundant elements, is kesterite Cu_2ZnSnS_4 (CZTS), showing a high absorption coefficient and a band gap around 1.4−1.5 eV. In particular, thanks to the ease of band-gap tuning by partial/total substitution of one or more of its elements, the high-band-gap kesterite derivatives have drawn a lot of attention aiming to find the perfect partner as a top absorber to couple with silicon in tandem solar cells (especially in a four-terminal architecture). In this work, we report the effects of the substitution of tin with different amounts of germanium in CZTS-based solar cells produced with an extremely simple sol−gel process, demonstrating how it is possible to fine-tune the band gap of the absorber and change its chemical−physical properties in this way. The precursor solution was directly drop-cast onto the substrate and spread with the aid of a film applicator, followed by a few minutes of gelation and annealing in an inert atmosphere. The desired crystalline phase was obtained without the aid of external sulfur sources as the precursor solution contained thiourea as well as metal acetates responsible for the in situ coordination and thus the correct networking of the metal centers. The addition of KCl in dopant amounts to the precursor solution allowed the formation of well-grown compact grains and enhanced the material quality. The materials obtained with the optimized procedure were characterized in depth through different techniques, and they showed very good properties in terms of purity, compactness, and grain size. Moreover, solar-cell prototypes were produced and measured, exhibiting poor charge extraction due to heavy back-contact sulfurization as studied in depth and experimentally demonstrated through Kelvin probe force microscopy.

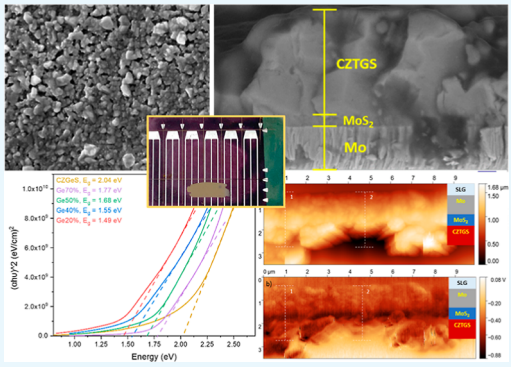

INTRODUCTION

Among the alternatives to silicon in the photovoltaic (PV) market, copper zin tin sulfide (CZTS) and its derivatives have drawn the attention of the scientific community, thanks to their structural similarity to the commercially available and well-performing copper indium gallium selenide (CIGS) solar cells.[1] This material is naturally present on earth with the name of crystalline kesterite and shows high absorption with an interesting band gap around 1.5 eV, together with a more affordable (in principle) production cost, thanks to cheaper and more earth-abundant elements compared to CIGS.[1,2]

In this context, record efficiencies of 12.6% for CZTS[3] and 12.6% for CZTSSe[4] have been achieved with "wet" deposition techniques which anyhow involve the use of hazardous chemicals, such as hydrazine. However, compared to conventional physical deposition procedures, chemical deposition methods have been proved to be the best candidate technology for the growth of kesterite thin films.

Despite the extremely positive results of the last decade, in the last few years, the research on the improvement of kesterite solar cells in terms of efficiency has somehow slowed down. This may be attributed to a plethora of unsolved issues regarding low open-circuit-voltage (V_{oc}) values, ease in the formation of secondary phases, as well as problems at the interfaces with the vicinal layers of the devices.[5−7] However, theoretical studies have demonstrated that it would be possible, in principle, to reach efficiencies of 20% or more by solving these issues.[8]

Despite this, the scientific research on this topic is still intense, especially thanks to the straightforward tuning of the

Received: March 24, 2022
Accepted: June 2, 2022
Published: June 29, 2022

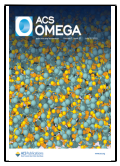

band gap of this class of materials by substituting partially or totally one or more components. This interest derives from the increasing need to evolve PV technology toward the tandem solar-cell architecture to overcome the Shockley limit and to boost well-performing and cheap solar devices such as the silicon ones.[9] In this context, the need to produce high-band-gap materials to be used as top cells in tandem architectures[10,11] has addressed the research toward the substitution of Zn with Fe, Mn, or Co in pure-sulfide CZTS solar cells, given that selenium is known for lowering the energy gap. However, no pronounced enhancement of the band gap has been reported for this methodology, which does not exceed values around 1.5−1.6 eV.[12−15] On the other hand, studies of Cu substitution with Ag or Li have been attempted successfully with the remarkable growth of the band gap (until 1.8 eV) but with the disadvantage to complicate the whole production procedure by using precursors that are more expensive or in other cases more difficult to handle.[16,17] Last but not least, in the last few years, Sn substitution with Ge have drawn the attention of the PV research community due to the extremely high band gap reachable, especially with the completely Ge-substituted pure-sulfide kesterite version. Several works report different compositions of $Cu_2ZnSn_xGe_{1-x}(S,Se)_4$ (CZTGSSe) and relate them to the optical and physical properties of the final absorber.[18−21] The results were interesting, especially in pure sulfide CZTGS where band-gap values ranging from 1.5 (for CZTS) to 2.1 eV (pure CZGS) have been registered.[22,23] Many different deposition techniques have been used, but no one allowed to reach remarkable results in terms of solar device performances for very high band gaps, exceeding 1.7 eV.

Encouraging results came from the mixed chalcogenide solar cells $Cu_2ZnSn_xGe_{1-x}(S,Se)_4$ (CZTGSSe) that reached efficiencies around 11−12% with a germanium content ≤ 40% (Sn ≥ 60%), thus also reporting low band gaps not suitable for tandem applications as top cells.[24] As for the pure sulfide version of the CZTGS material, very low efficiencies have been reported for a high germanium content,[23] and the current record for fully germanium-substituted kesterite CZGS is around 0.7%.[22] However, except for the PV field, other interesting applications of these materials can also be investigated, such as CO_2 reduction, which had already been reported with extremely good results by Ikeda and coworkers.[22]

In this work, we wanted to deeply investigate the nature of the pure sulfide alloy, leading to high energy gaps, to provide new outcomes for the tandem PV application field. To do so, we adapted our simple methodology, recently described elsewhere,[25,26] to produce a small library of CZTGS samples with different tin−germanium contents to fine-tune the band gap of the material for the future tandem device applications. This procedure allowed us to avoid industrially nonappealing deposition machines and prevent the wastage of raw materials compared to other techniques. Moreover, a feasible methodology to compensate for the germanium loss during annealing was optimized, and the beneficial effect of introducing dopant amounts of KCl in the precursor solution was confirmed in terms of grain growth and passivation. The good quality of the material was proved by several complementary analytical techniques, and a corresponding PV device was produced and characterized.

MATERIALS AND METHODS

Substrate Preparation. Commercially available soda-lime glass (SLG) was cleaned in an ultrasonic bath in the following sequence: mucasol solution (15′), deionized water (3 × 15′), acetone (15′), and ethanol (15′) and then one by one dried in vacuum. The so-cleaned substrates were coated with a Mo thin film deposited by magnetron DC sputtering in two steps, with a final thickness of 1.1 μm.

Preparation of Solutions with Different Ge Concentrations. To prepare the CZTGS precursor solutions, copper(II) acetate hydrate $Cu(CH_3COO)_2{\cdot}H_2O$ [0.27 M]; tin(II) chloride dihydrate $SnCl_2{\cdot}2H_2O$ and/or $GeCl_2{\cdot}$dioxane (total concentration, 0.16 M, see Table 1 for details]; zinc(II) acetate dihydrate $Zn(CH_3COO)_2{\cdot}2H_2O$ [0.19 M]; and thiourea $SC(NH_2)_2$ [3.0 M] were dissolved in dimethylsulfoxide (DMSO). The final sol−gel inks were obtained after 48 h under stirring at room temperature with a pale-yellow and crystal-clear appearance.

Table 1. Stoichiometric Composition of Precursor Solutions for All Ge−Sn Compositions

	$SnCl_2{\cdot}H_2O$ [M]	$GeCl_2{\cdot}$dioxane [M]	total [M]
Cu_2ZnSnS_4	0.160		0.160
$Cu_2ZnSn_{0.8}Ge_{0.2}S_4$	0.128	0.032	0.160
$Cu_2ZnSn_{0.6}Ge_{0.4}S_4$	0.096	0.064	0.160
$Cu_2ZnSn_{0.5}Ge_{0.5}S_4$	0.080	0.080	0.160
$Cu_2ZnSn_{0.3}Ge_{0.7}S_4$	0.048	0.112	0.160
Cu_2ZnGeS_4		0.160	0.160

Deposition and Thin-Film Growth. The precursor solution was drop-cast directly onto a 3 cm^2 ozone-cleaned Mo-SLG substrate with the help of a micropipette. The droplet spreading was made with the aid of a film applicator Zehntner ZAA 2300. Each layer deposition was followed by 30′ of gelation and then annealing in a tubular oven under an inert atmosphere (Ar) starting from RT and rising to 570 °C with a rate of 18.2 °C/min, followed by a plateau at 570 °C for 15 min; after that the samples were left to cool down naturally under Ar. This procedure was repeated four times to reach the desired thickness (about 1.5 μm). Details of the volume and blade thickness for each deposited layer are available in Table 2.

Table 2. Detailed Volume and Blade Thickness for Each Deposited Layer with a Film Applicator[a]

	volume (μL/cm^2)	blade thickness (mils)
1st layer	5.3	4
2nd layer	5.3	4
3rd layer	6.0	5
4th layer	6.7	6

[a]Where 1 mils = 25.4 μm.

Characterization. Crystallographic data of the samples were obtained by X-ray diffraction (XRD) of thin films, performed using a Rigaku Miniflex 600 apparatus (F.F tube 40 kV, 15 mA, DS/SS = 1.25°, RS = 0.3 mm, HyPix-400 MF 2D—HPAD). Raman spectra were obtained using a Jasco Ventuno μ-Raman instrument with a Peltier-cooled charge-coupled device (CCD) camera (operating temperature: −50 °C) and a He−Ne laser (wavelength, 632.8 nm; power density, 6 kW/cm^2). Calibration of Raman was done using a single-

https://doi.org/10.1021/acsomega.2c01786
ACS Omega 2022, 7, 23445−23456

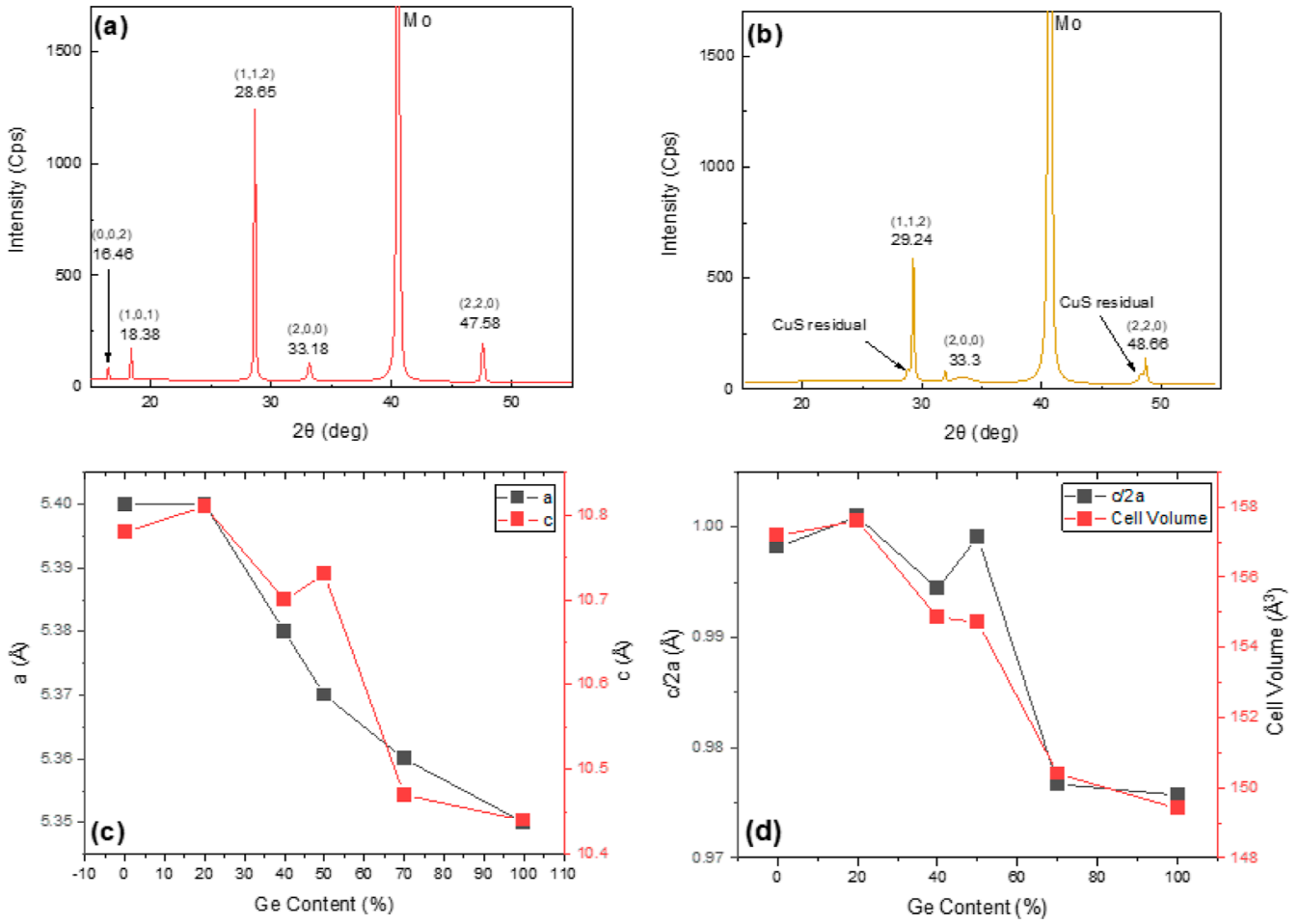

Figure 1. (a) $Cu_2ZnSn_{0.8}Ge_{0.2}S_4$ XRD pattern showing only the peaks of the material with no secondary phases detectable; (b) Cu_2ZnGeS_4 XRD pattern showing the peaks of the material in presence with CuS residual secondary phase; (c) lattice parameters variation vs Ge content; and (d) cell distortion and cell volume vs Ge content.

crystal Si reference sample before each measurement by shifting the position of the Si main peak at 520.65 cm^{-1}. The morphology of the samples and the compositional profile were studied both in planar and cross-sectional view by Tescan VEGA TS5136XM scanning electron microscopy (SEM) equipped with energy-dispersive spectroscopy (EDS) or by a Gemini 500 Zeiss equipped with a QUANTAX EDS 4000, EBSD, STEM. All optical transmission measurements of the materials were carried out in the 350−2500 nm spectral region using a Jasco V-770 UV−vis−NIR spectrophotometer. Photoluminescence (PL) spectra were recorded in the 550−1000 nm spectral range from 77 to 300 K. All PL measurements were performed through a Horiba T6400 spectrometer equipped with a 1800 lines/mm grating and a Si-CCD detector. A duplicate solid-state Nd:YAG laser with λ_{exc} = 532 nm was used as the excitation source. Data analysis was performed by OriginPro 2020b. Kelvin probe force microscopy (KPFM) measurements were performed under ambient conditions using a scanning probe microscopy system from AIST-NT (TRIOS platform) in the two-pass scanning mode where the second pass was performed at a constant distance of 30 nm from the sample surface. To measure the surface potential, ARROW EFM conductive tips with a PtIr coating at a resonance frequency of 75 kHz were used.

Device Preparation and Measurements. The PV cells were scribed manually into small, isolated areas of 0.15 cm^2 and were produced with a standard architecture. The CdS buffer layer with ∼80 nm thickness was deposited by chemical bath deposition, a thin i-ZnO layer (70 nm) was deposited by RF sputtering, and Al-doped ZnO (AZO) was chosen as top contact and deposited by DC pulsed (2 kHz) sputtering with a thickness of 350 nm. Finally, the devices were completed by evaporation of an Al grid (thickness ∼ 500 nm). CZTGS-based solar cells were characterized using a 500 W xenon light source (ABET Technologies Sun 2000 class ABA Solar Simulator), calibrated to AM 1.5 (100 mW/cm^2) by a reference Si cell photodiode and an IR cut-off filter (KG-5, Schott) to reduce the mismatch between the simulated light and the AM 1.5 spectrum in the 350−750 nm range. The IV curves were measured by applying an external bias to the device and recording the generated photocurrent with a Keithley model 2400 digital source meter. External quantum efficiency (EQE) measurements were recorded using a SpeQuest quantum efficiency system, as a function of excitation wavelength by using a monochromator (Omni 300 LOT ORIEL) with a single grating in Czerny−Turner optical design, in AC mode with a chopping frequency of 88 Hz.

RESULTS AND DISCUSSION

The properties of the so-produced samples were extensively investigated to control the quality quaternary phase of CZTGS. The characterization of the material was done immediately

https://doi.org/10.1021/acsomega.2c01786
ACS Omega 2022, 7, 23445−23456

after the deposition and the corresponding annealing of the last step.

First, XRD measurements were carried out, from which good crystalline quality of the thin film can be inferred. As indicated in Figure 1, a typical XRD pattern of the CZTGS complete layer shows sharp and well-defined peaks related to the pure phase of the corresponding desired composition as reported elsewhere in the literature.[27]

No secondary phases can be detected for low germanium contents. The intense peak present at $2\theta = 40.0°$ is attributed to the Mo thin film used as a back contact for the CZTGS deposition. For high germanium contents, it is possible to notice the presence of broad shoulders at 28.6° and 47.5° which can be attributed to the CuS residual secondary phase. This can be inferred to a loss of germanium during the annealing at high temperatures (due to its volatility), occurring only at high-Ge contents (with Ge ≥ 70% and Sn ≤ 30%), which was proved subsequently by EDS measurements (as described in the following paragraphs).

Moreover, by analyzing the trend of lattice parameters of the cell unit, it is possible to appreciate a progressive cell distortion when Ge content exceeds 50%, as well as a progressive cell volume decrease under the same conditions, with minimum volume reached for the completely Ge-substituted compound. These data agree with the smaller atomic radius of Ge compared to that of Sn, driving the cell unit toward smaller values but still retaining kesterite form.

In addition, in Figure 2, it is possible to appreciate the progressive shift of the kesterite main peak, corresponding to

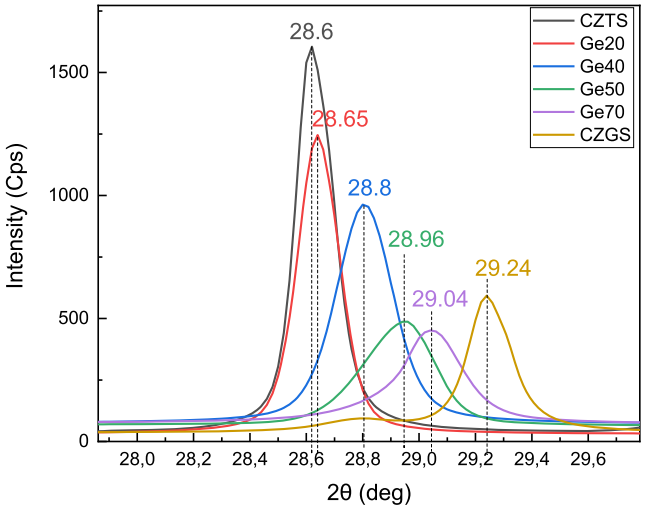

Figure 2. XRD pattern main peak (1,1,2) shifting depending on Ge−Sn content.

the orientation plane (1,1,2), ranging from 28.6° for pure CZTS to 29.24° for pure CZGS as expected from the literature.[27]

Unfortunately, the crystal structure of CZTGS is comparable to many possible secondary phases obtainable as byproducts during the formation of the quaternary kesterite phase. For this reason, a stand-alone XRD analysis is not enough to determine univocally the crystalline quality of the material, pointing out the necessity to use other complementary techniques such as Raman spectroscopy.

In the Raman spectrum (Figure 3a), the presence of a pure phase of germanium-derived kesterite is confirmed by its typical peaks for all the different germanium−tin concentrations examined.[27−29] In particular, as described by Garcia-Llamas and coworkers in their accurate Raman study of germanium-substituted CZTS with different compositions, it is possible to appreciate the main peak split (Figure 3b), generated by the coexistence of Sn and Ge atoms into the crystal structure, when the Ge/Sn ratio reaches 70:30.[27,30,31] After that ratio, the doublet reunifies in a sole signal shifted to higher wavenumbers, as demonstrated also by the convolution of the main peak shown in Figure 3c. Finally, the characteristic peaks of other known detrimental phases are not detectable in the spectra.

Thanks to these data, we can conclude that in our conditions of growth (Table 1), the kesterite CZTGS phase is formed, thanks to the desired coordination of the precursors in solution and the right timing in terms of the gelation process and thermal annealing.

The morphology and composition of all the samples have been investigated by SEM and EDS measurements. By these two techniques emerged a double issue: first of all, the morphology indicated a very small grain dimension (100 to 200 nm) as well as the presence of voids and/or cavities (Figure 4). Moreover, from EDS analyses emerged a non-negligible Ge loss (around 25% of the desired Ge content was missing) for the Ge-rich samples when starting Sn/Ge mixtures exceed 30:70, probably due to the high volatility of Ge at the annealing temperatures. Specifically, for the $Cu_2ZnSn_{0.3}Ge_{0.7}S_4$ sample, the metal ratio resulted in Cu/(Zn + Sn + Ge) = 0.81 ± 0.02, Zn/(Sn + Ge) = 1.51 ± 0.08, and Ge/(Ge + Sn) = 0.55 ± 0.05. While for CZGS, the metal ratio resulted in Cu/(Zn + Ge) = 0.87 ± 0.03 and Zn/Ge = 1.41 ± 0.07.

To solve the composition problem for mixtures with Ge ≥ 70% and Sn ≤ 30%, a new solution was prepared for the high-Ge-content samples ($Cu_2ZnSn_{0.3}Ge_{0.7}S_4$ and Cu_2ZnGeS_4) with the same methodology described above, but using an excess of 50% of $GeCl_2$·dioxane moles compared to the stoichiometric, as described in Table 3 (specifically 0.168 M instead of 0.112 M for $Cu_2ZnSn_{0.3}Ge_{0.7}S_4$ and 0,24 M instead of 0,16 M in the case of Cu_2ZnGeS_4).

Moreover, 0.04 M KCl was added to help with the grain growth and passivation, as well as to minimize the voids and lead to a more compact morphology of the material, having already proved and described recently the beneficial effect of this procedure on CZTS samples prepared with the same methodology.[25] In fact, during the annealing, KCl converts into K_2S, helping the coalescence of vicinal grains and thus leading to a more compact material.[32]

In Figure 5a, it is possible to appreciate the morphology improvement, thanks to the KCl addition, where the material results more compact and with respectable grain dimensions ranging between 400 nm and 1 μm. Moreover, from the cross-sectional image (Figure 5b), it is possible to notice the absence of voids at the interface with the back contact or between vicinal grains, as well as a final absorber thickness around 1.7 μm, as desired. However, it is also possible to notice a considerable thickness (about 200 nm) of the detrimental MoS_2 layer, resulting as a byproduct of Mo back contact sulfurization under the extremely harsh annealing conditions necessary to obtain the correct CZTGS phase formation. On the other hand, from EDS measurements, it was possible to confirm the Ge loss compensation, thanks to the new solution previously described in Table 3. In fact, the new metal ratio for $Cu_2ZnSn_{0.3}Ge_{0.7}S_4$ resulted in Cu/(Zn + Sn + Ge) = 0.77 ±

https://doi.org/10.1021/acsomega.2c01786
ACS Omega 2022, 7, 23445−23456

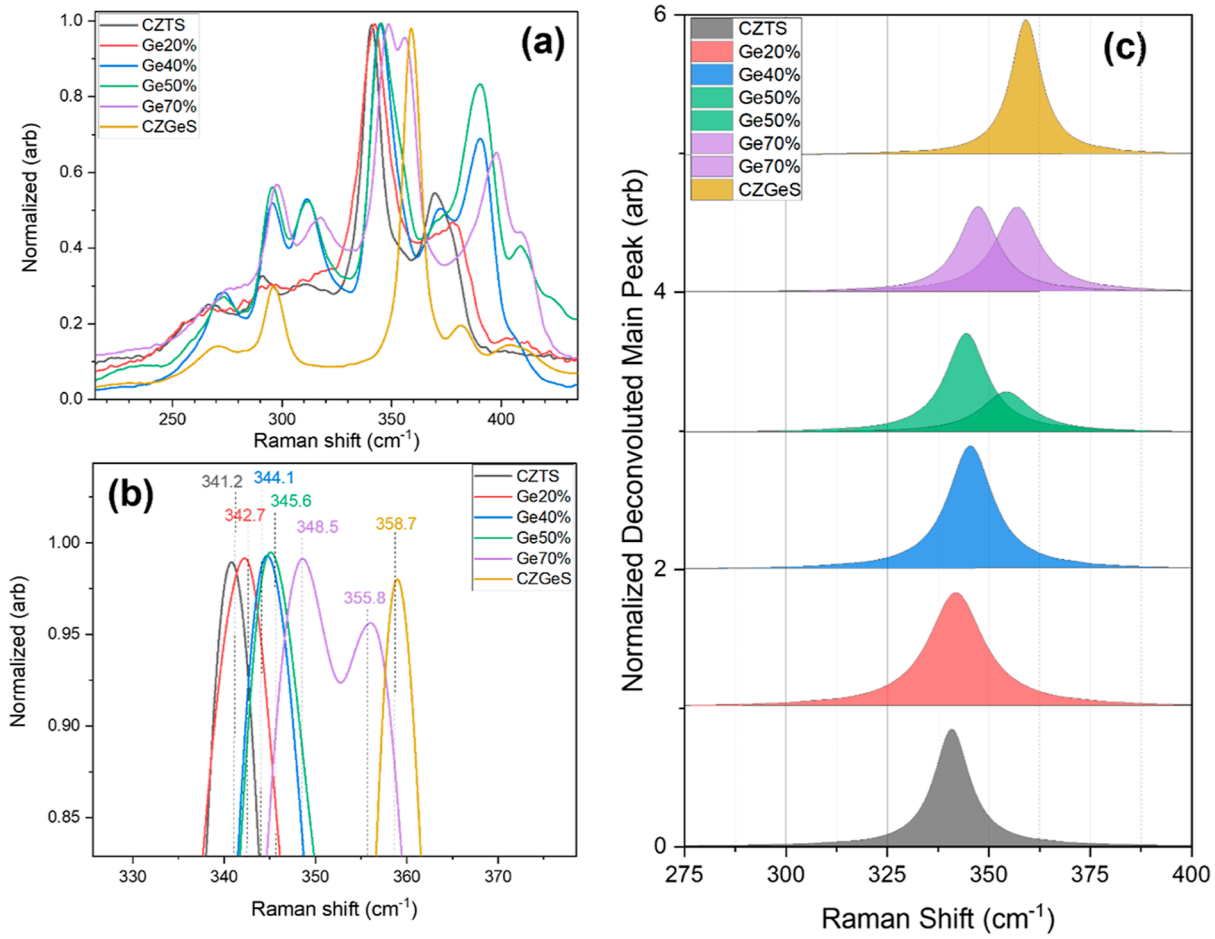

Figure 3. (a) Stacking of Raman spectra for all the Ge−Sn compositions; (b) Raman spectra main peak shifting and splitting depending on Ge−Sn content; and (c) convolution of the Raman spectra main peak depending on Ge−Sn content.

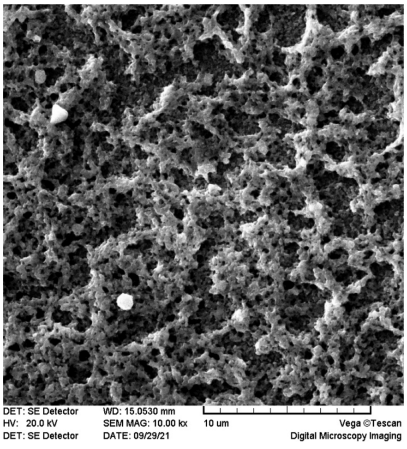

Figure 4. SEM planar view of the $Cu_2ZnSn_{0.3}Ge_{0.7}S_4$ sample with a predominance of voids and cavities.

Table 3. Corrected Composition of Precursor Solution for High-Ge-Content Samples: $Cu_2ZnSn_{0.3}Ge_{0.7}S_4$ and Cu_2ZnGeS_4

	$SnCl_2$ H_2O [M]	$GeCl_2$·dioxane [M]	Total [M]
$Cu_2ZnSn_{0.3}Ge_{0.7}S_4$	0.048	0.168	0.216
Cu_2ZnGeS_4		0.24	0.24

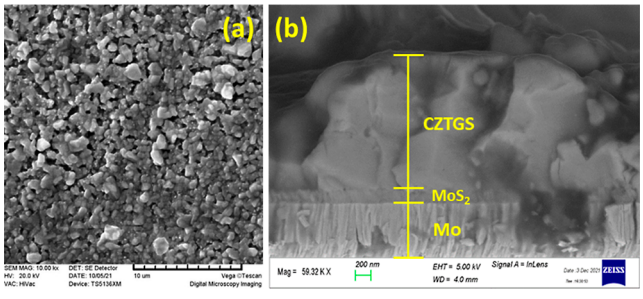

Figure 5. (a) SEM planar view of the $Cu_2ZnSn_{0.3}Ge_{0.7}S_4$ sample after Ge-loss compensation and KCl addition with well-grown and compact morphology. (b) SEM cross-section of the $Cu_2ZnSn_{0.3}Ge_{0.7}S_4$ sample after Ge-loss compensation and KCl addition with well-grown and compact morphology; heavy formation of the MoS_2 layer is well-visible and with an approx. thickness of 200 nm.

0.08, Zn/(Sn + Ge) = 1.05 ± 0.09, and Ge/(Ge + Sn) = 0.71 ± 0.05, as desired. While for CZGS, the metal ratio resulted in Cu/(Zn + Ge) = 0.78 ± 0.06 and Zn/Ge = 1.08 ± 0.09.

Therefore, the addition of exceeding amounts of germanium compared to the stoichiometric together with dopant amounts of KCl has been proved to be beneficial to reaching the target composition, grain size, and thin-film density.

All the samples already described were also directly grown on a SLG substrate to investigate the optical properties of the thin films by UV−vis spectroscopy. Transmittance and

https://doi.org/10.1021/acsomega.2c01786
ACS Omega 2022, 7, 23445−23456

reflectance measurements were acquired to calculate the absorption coefficient (α) to which to apply the Tauc relation to calculate the optical band gap.[33] To do so, the optimized materials have been used, in particular: Ge20%, Ge40%, and Ge50% have been produced with the main recipe (Table 1) while Ge70% and CZGS with the recipe corrected to avoid Ge losses (Table 3).

Tauc's plot of all the compositions has been reported in Figure 6 and reveals the desired and expected band-gap tuning, matching with other examples described in the literature.[22,23]

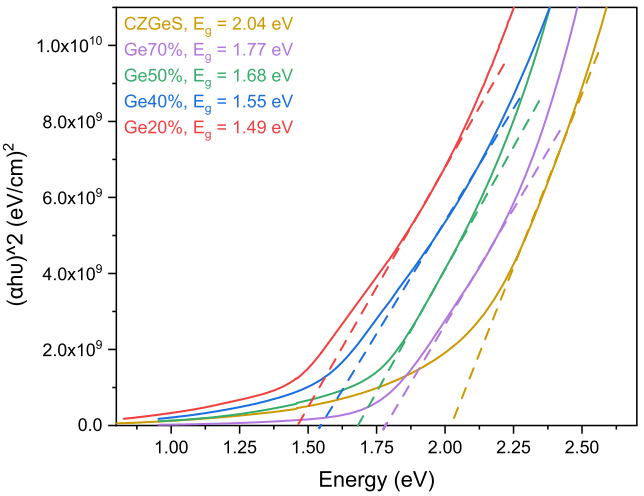

Figure 6. Tauc's plot of all the samples at different Ge/Sn compositions shows the expected trend for the band gap. The transmittance and reflectance have been measured on the optimized materials deposited on SLG, in particular: Ge20%, Ge40%, and Ge50% have been produced with the main recipe (Table 1) while Ge70% and CZGS with the recipe corrected to avoid Ge losses (Table 3).

Among all the samples, the one with 70% of Ge content ($Cu_2ZnSn_{0.3}Ge_{0.7}S_4$), thanks to its band gap of 1.77 eV, has been chosen as the best candidate absorber for a top cell in a four-terminal tandem device architecture, involving c-Si as the bottom cell. In fact, it is reported that for this kind of specific tandem architecture (actually the easiest to produce on the laboratory scale), a band gap between 1.7 and 1.8 eV for the top cell is desired.[34−37]

PL spectroscopy allows us to investigate the defect states within the band gap. PL emissions at room temperature of samples with Ge40%, Ge50%, and Ge70% substitution have been compared in Figure 7a. The mismatch in energy between the optical band gap and the PL peak position is typical for sulfur-based kesterite, and it has been ascribed to optoelectronically active defects in the band gap close to band edges.[38,39] $Cu_2ZnSn_{0.5}Ge_{0.5}S_4$ and $Cu_2ZnSn_{0.3}Ge_{0.7}S_4$ have a reduced mismatch of about 0.06 eV, and meanwhile, the 40% Ge substituted shows an increase of the band gap of 0.1 eV, indicating a high density of thermalized defects.[40] It has to be highlighted that the PL intensity of the Ge50% and Ge40% is less than the 25% of the intensity of the Ge70%, suggesting an increase of nonradiative transitions due to a high defect density.[41] A PL study varying excitation power and temperature can identify the radiative recombination mechanisms operating in semiconductors.[42] The PL spectra varying temperatures are shown in Figure 7b−d. As the temperature decreases, the 40- and 50%-substituted thin films have a dramatic quenching of the main emission peak; meanwhile, one at about 1.4 eV arises. The 70% Ge-substituted thin film has the emission peak located at about 1.7 eV and as expected, the bands' shape is asymmetrical, showing a broader decay at low energies and a sharper one at high.[43] Therefore, PL analysis suggested that the compound with the lower number of defects acting as charge traps is $Cu_2ZnSn_{0.3}Ge_{0.7}S_4$.

$Cu_2ZnSn_{0.3}Ge_{0.7}S_4$ was chosen as the most promising candidate to produce a solar-cell prototype, so we analyzed the PL trend in temperature (Figure 8a) and investigated the PL emission at 77 K (Figure 8b) varying the excitation power. The reported shift to lower energies with increasing temperature has not been revealed in $Cu_2ZnSn_{0.3}Ge_{0.7}S_4$. A slight shift over higher energy has instead been measured (Figure 8a), which, according to the literature, could be ascribed to an increasing concentration of free holes and electrons.[42] On the other hand, the emission at 1.4 eV is recorded also for the 70% Ge-substituted sample. This contribution has been previously detected in CZTS thin films and single crystals and has been ascribed to deep donor-deep acceptor pair defects (interstitial Zn atom as deep donor defect and Cu_{Zn} as the acceptor one).[43] Moreover, it has to be noted that the main PL peak blue-shifts by increasing excitation power: this behavior can be ascribed to a band-to-impurity (BI; free electrons recombine in acceptor states) or a band-to-tail (BT; recombination of holes with free electrons from the conduction band in localized states of the valence band tail) transitions.[42] To confirm our findings, we performed the deconvolution of the PL spectra, depicted in Figure 8c. We plotted the PL intensity as a function of the excitation power to determine the power coefficient k: when it is lower than one, the associated recombination is related to defect states localized within the energy gap.[42] At 77 K, $Cu_2ZnSn_{0.3}Ge_{0.7}S_4$ displays a k of 0.40 ± 0.20 (Figure 8d), confirming that detrimental energy levels are localized within the band gap. As reported in the literature for kesterite,[42] in compounds with tin partially substituted by germanium, the main peak position has a blue shift increasing the excitation power, which is correlated with radiative transitions from the conduction band to impurities or band-tail energy states. The parameter β, that is, the decay rate in Figure 8e, for $Cu_2ZnSn_{0.3}Ge_{0.7}S_4$ is 41.0 ± 19.1 meV/decade. Oueslati reported a β increase by replacing Ge with Sn. In our case, a smaller value of k and a bigger value of β, compared to the ones reported in the literature, can be ascribed to the highly disordered structure, induced by the fast cooling after the annealing.[42]

Therefore, the defects can be ascribed to the Ge introduction in the CZTS structure that, as reported for CZTGSSe,[42] increases the disorder degree, leading to the formation of localized acceptor levels such as Zn_{Sn} with Zn_{Ge} or Zn_{Sn}, that act as traps for free electrons. Since in our 70% Ge-substituted samples the shift is just over half of the quoted value, we can deduce that the BT or BI recombinations are present but lower than those reported so far in the literature.[42]

The so-produced $Cu_2ZnSn_{0.3}Ge_{0.7}S_4$ samples have been finalized as devices with the procedure already described in the Materials and Methods. The resulting solar cells have been measured under the dark and illuminated conditions, with the aid of a solar simulator and their EQE was also registered. In Figure 9a, it is possible to observe the dark and illuminated JV curves of our typical CZTGS solar cell, where the very bad charge generation and/or extraction emerges from the cell parameters (V_{oc} = 22.3 mV, J_{sc} = 2.7 mA/cm^2, FF = 16.4%, and

https://doi.org/10.1021/acsomega.2c01786
ACS Omega 2022, 7, 23445−23456

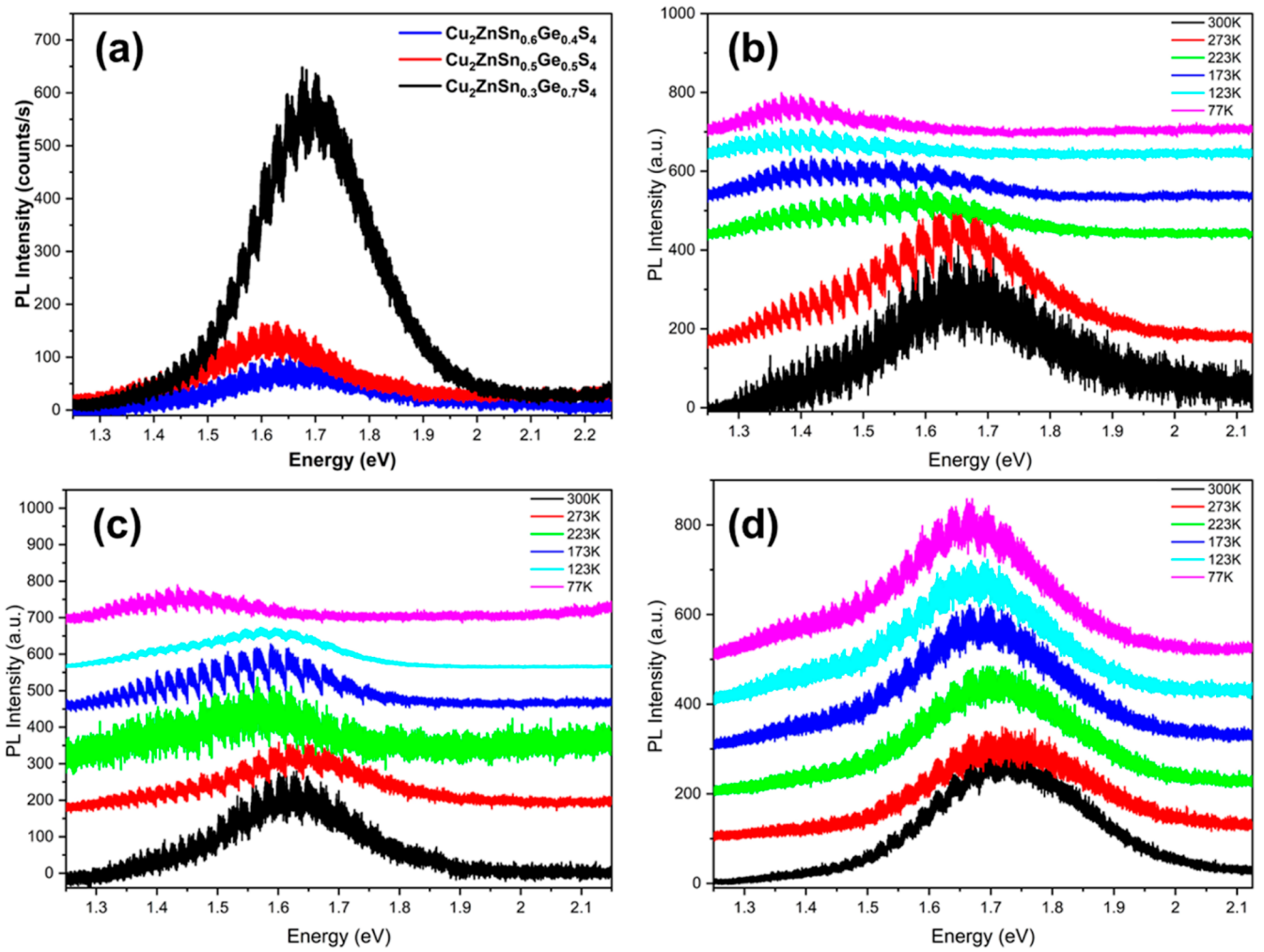

Figure 7. (a) PL measurements of $Cu_2ZnSn_{0.6}Ge_{0.4}S_4$, $Cu_2ZnSn_{0.5}Ge_{0.5}S_4$, and $Cu_2ZnSn_{0.3}Ge_{0.7}S_4$ at room temperature (excitation power of 1.2×10^8 W/cm^2); (b) PL measurements of the $Cu_2ZnSn_{0.6}Ge_{0.4}S_4$ sample at different temperatures; (c) PL measurements of the $Cu_2ZnSn_{0.5}Ge_{0.5}S_4$ sample at different temperatures; and (d) PL measurements of the $Cu_2ZnSn_{0.3}Ge_{0.7}S_4$ sample at different temperatures.

η = 0.01%). In fact, by measuring the sulfurized back contact with the four-wire technique, the resistivity ranged around 90−120 kΩ, probably due to the extremely high Mo sulfurization occurring during the annealing at very high temperatures (570 °C) as also depicted in the SEM section-image shown previously in Figure 5b.

The EQE is depicted in Figure 9b: the curve in the 300−550 nm region shows loss due to the parasitic absorption from the buffer layer (CdS absorption is around 530 nm) and from the window layers (i-ZnO/AZO layers cut the wavelengths minor than 380 nm).[30] The low response in the 400−600 nm range is attributed to the charge recombination related to trap states located at the interfaces and to the nonideal band alignment of a wide-band-gap absorber with the CdS buffer layer.[44] The integrated J_{sc} is about 3 mA/cm^2, and it nicely matches the current density calculated from the JV curve measured at AM1.5. The band gap was assessed by plotting $[(h\nu \cdot \ln(1 - \mathrm{EQE})]^2$ versus $h\nu$, where $h\nu$ is incident photon energy.[45] By using linear extrapolation, the band gap was determined to be 1.77 eV (inset, Figure 9b), which is coherent with the value obtained from the absorption spectroscopy analysis. In general, the EQE measurements (Figure 9b) demonstrate how the shape of the curve matches the nature of this high-band-gap absorber. Moreover, it points out a good bulk nature with few recombinations at this level, suggesting that low efficiency is mainly related to recombination that takes place probably at the interfaces. In particular, this issue is related to the back contact due to the bulky MoS_2 presence already described in other works of our research group[11,25] and to the well-known bulk features typical of the kesterite phase and also revealed by PL analysis.[46]

To investigate the CZTGS devices, KPFM measurements have been performed on the cross-section of the device. KPFM measurements were performed under ambient conditions using a scanning probe microscopy system from AIST-NT (TRIOS platform)[47] in two-pass scanning mode where the second pass was performed at a constant distance of 30 nm from the sample surface. To measure the surface potential, ARROW EFM conductive tips with a PtIr coating at a resonance frequency of 75 kHz were used.

A smooth topography is an almost necessary feature for reasonable KPFM measurements. However, the first-stage analysis revealed that the cross-section was not homogeneous and presented high roughness, due to the nonoptimized cross-sectional preparation procedure and the deposition process, respectively.

Therefore, the analysis was executed in frequency modulation KPFM (FM-KPFM)[48] with a low scanning rate of 0.1

https://doi.org/10.1021/acsomega.2c01786
ACS Omega 2022, 7, 23445−23456

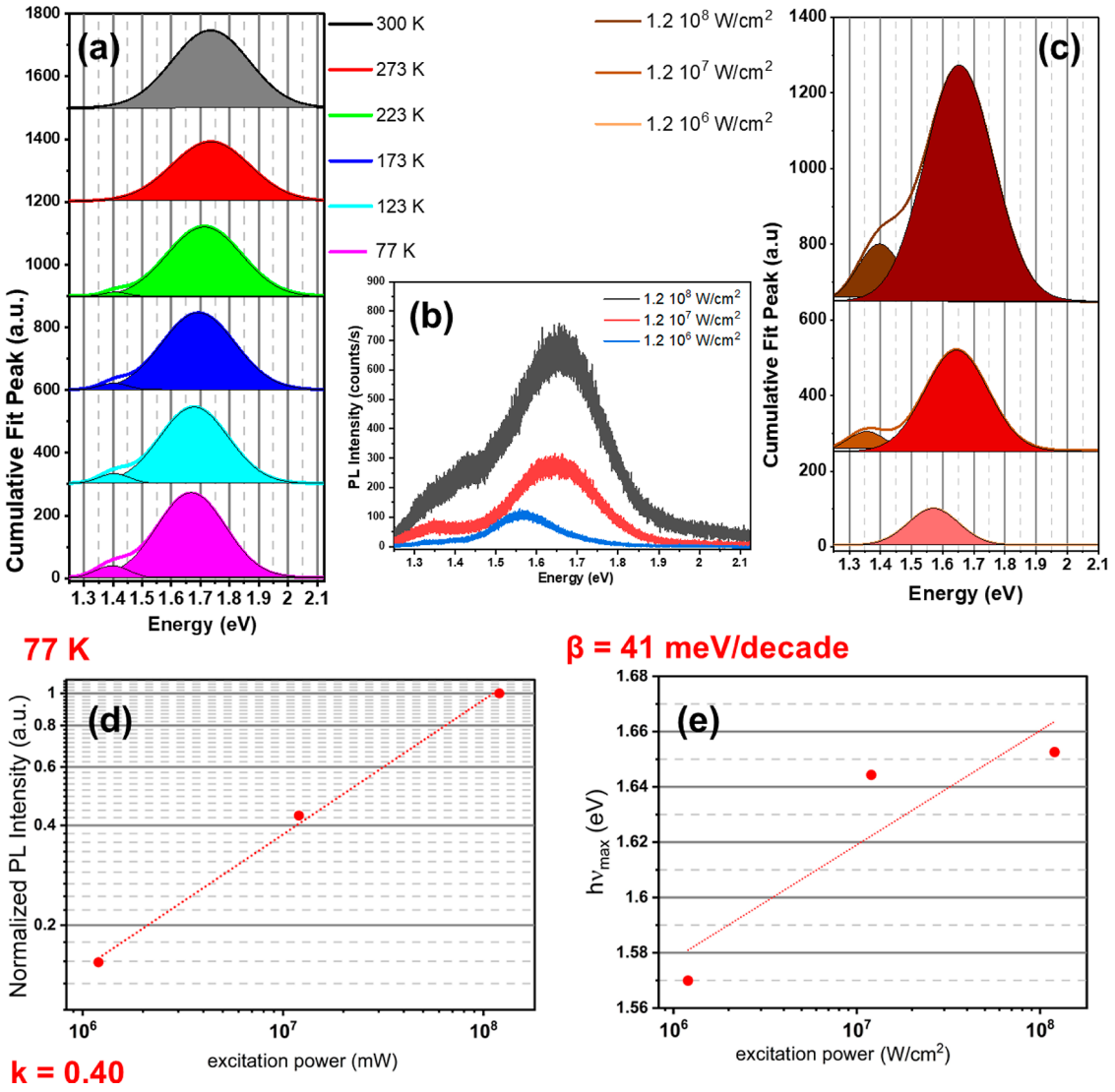

Figure 8. (a) PL cumulative fit peak of the $Cu_2ZnSn_{0.3}Ge_{0.7}S_4$ sample at different temperatures; (b) PL measurements of the $Cu_2ZnSn_{0.3}Ge_{0.7}S_4$ sample with different excitation powers; (c) PL cumulative fit peak of the $Cu_2ZnSn_{0.3}Ge_{0.7}S_4$ sample with different excitation powers; (d) linear fitting of PL intensity vs excitation power at 77 K; and (e) linear fitting of integrated PL intensity vs excitation power.

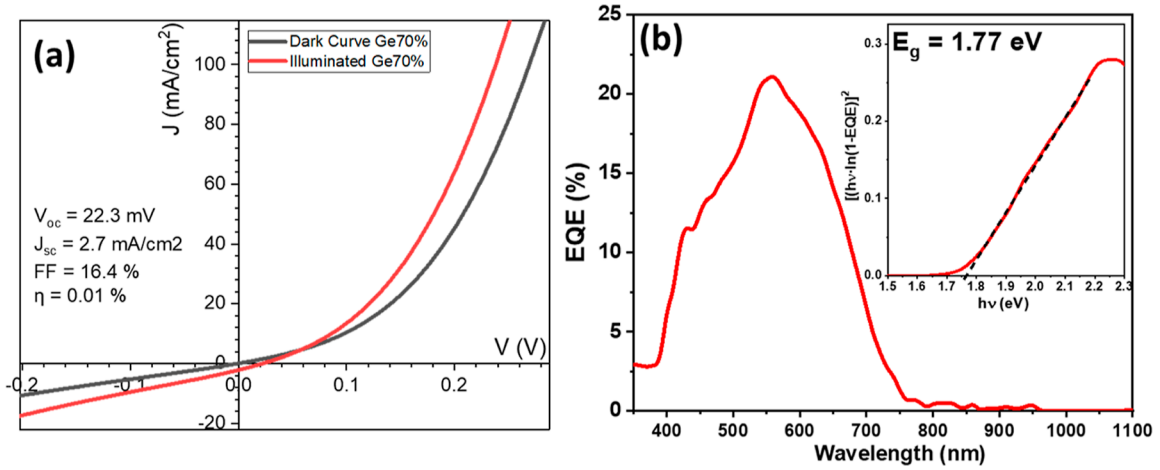

Figure 9. (a) JV curve of the $Cu_2ZnSn_{0.3}Ge_{0.7}S_4$ sample in the dark and illuminated mode showing poor charge extraction and (b) EQE curve of the $Cu_2ZnSn_{0.3}Ge_{0.7}S_4$ sample showing good shape; (inset) band gap value calculated from EQE, matching with the one calculated by the Tauc plot reported in Figure 6.

https://doi.org/10.1021/acsomega.2c01786
ACS Omega 2022, 7, 23445−23456

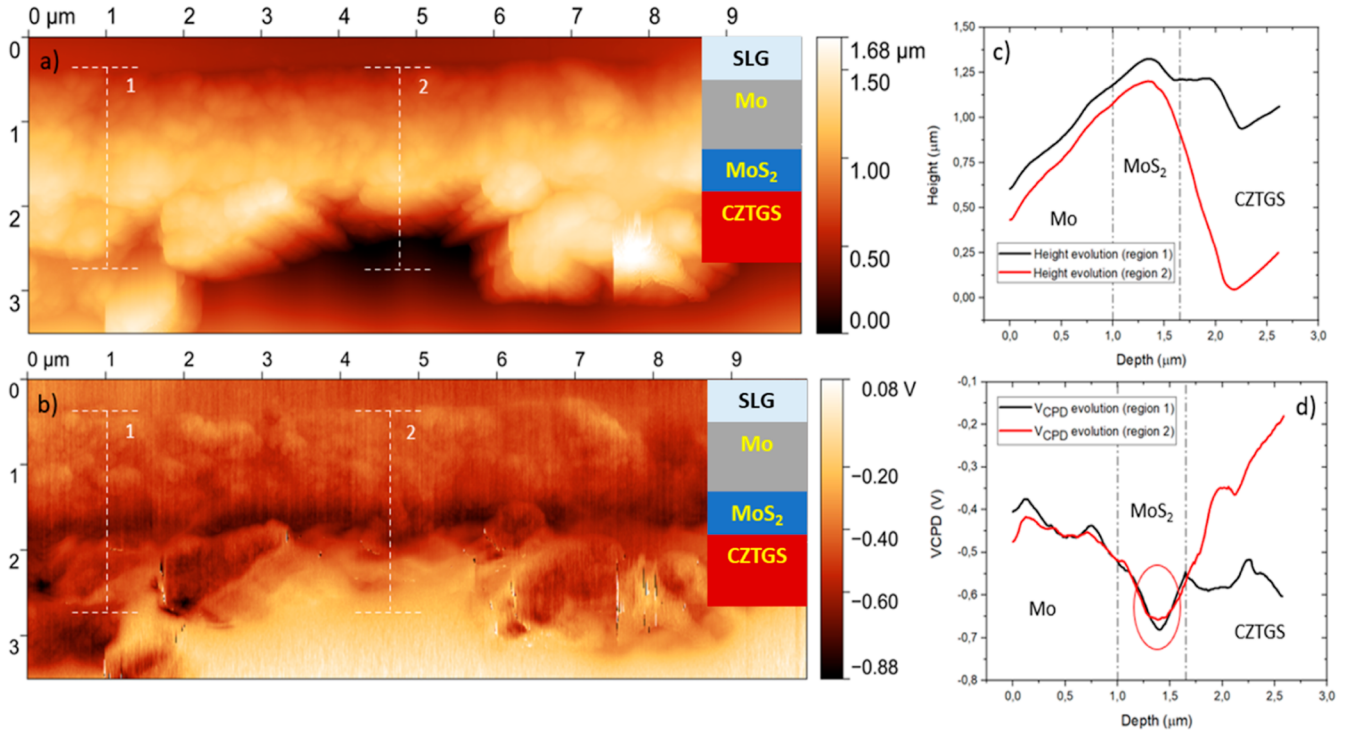

Figure 10. FM-KPFM measurement of the surface cross-section of the CZTGS device. The topography (a) and the simultaneous VCPD image (b). The profiles in (c,d) show an average value of the data along with the topography and VCPD image, respectively. The profiles correspond to the two regions identified by the dotted white segment.

Hz to mitigate the effect of the surface roughness and inhomogeneities.

The topography and the associated contact potential difference (VCPD) image are reported in Figure 10a. The topography shows the solar cell structure up to the CZTGS active layer. The other layers which comprise the device are not well-evidenced due to the nonoptimized cross-sectional process. The simultaneously measured VCPD image reveals a region in which the VCPD drops, as highlighted by the red circle in the extracted profile in Figure 10d. This region corresponds to the interface between Mo and the CZTGS absorber and can be related to the massive formation of MoS_2 during the annealing process. Note that FM-KPFM allowed to avoid a topographical imprint on the VCPD image, as shown in the profile in Figure 10.

Similarly, the evolution of the work function (WF) follows the one of the VCPD[49] since

$$V_{CPD} = \frac{\Phi_{tip} - \Phi_{sample}}{-e}$$

so that a drop in VCPD corresponds to an increase in the WF.

This feature, already detected also in the SEM cross-sectional image (Figure 5b), is the proof of the charge extraction problems already supposed previously in this work and also encountered and detected by fitting and simulations in previous works of the research group on samples grown under similar conditions.[11,25] Therefore, despite the pure-phase absorber production with the desired optical and morphological properties, the resulting insulating MoS_2 layer generated by the heavy back contact sulfurization hinders the proper charge extraction from the device.

CONCLUSIONS

In conclusion, in this work, we demonstrate that our simple and cheap sol−gel process can successfully lead to good-quality CZTGS thin films with different Ge−Sn compositions to fine-tune the band gap of kesterite, aiming to make it suitable as a top cell for a four-terminal tandem application coupled with c-Si cells. We demonstrate that with our methodology, it is possible to easily compensate for Ge losses (experimentally registered only with high Ge contents, Ge ≥ 70%) just by adjusting the precursor solution composition. In addition, our procedure allows us to avoid industrially nonappealing deposition machines (such as sputtering) and to prevent the wastage of raw materials compared to other wet deposition techniques (such as spin coating and spray pyrolysis). The crucial role of precursor metal acetate salts, thiourea, and potassium chloride, already successfully used and described for our CZTS thin films, matches perfectly even with the germanium-substituted forms of kesterite, even in different Sn/Ge ratios, leading to a good-quality material that is compact with respectable grain size and no detectable secondary phases or cavities.

The corresponding solar devices unfortunately did not show the expected results due to a very bad charge extraction. However, it has been experimentally demonstrated by accurate KPFM studies that the reason for this bad device behavior is the highly sulfurized Mo back contact where a drop in potential takes place, practically arresting the charge extraction. However, the good shape of the EQE curves indicates the absence of significant recombination losses in the bulk and matches the nature of such a high-band-gap absorber, where only a small portion (at low wavelengths) of solar radiation can be harvested. It has to be said that, in this context, for the pure sulfide version of the material CZTGS, very low efficiencies

https://doi.org/10.1021/acsomega.2c01786
ACS Omega 2022, 7, 23445−23456

have been reported for high germanium contents (E_g > 1.7 eV),[23] and the current record for fully germanium-substituted kesterite CZGS is around 0.7%, with a harsh and wasteful procedure carried out by spray pyrolysis and annealing at 600 °C.[22] With our outcomes, we aim to highlight the importance of the research on the top absorbers for four-terminal tandem solar architectures based on absorbers made of earth-abundant elements. In particular, $Cu_2ZnSn_{0.3}Ge_{0.7}S_4$, with E_g = 1.77 eV, could be the best candidate for a four-terminal tandem application coupled with c-Si cells, thanks to our easy, straightforward, and cheap fabrication process. Considering this as a proof-of-concept study, there is margin for the process improvement, especially thanks to back contact engineering. For example, by adding few nanometers of the TiN window layer by atomic laser deposition on the back contact, as well as by adopting faster annealing procedures with the aid of rapid thermal processing, it would be possible to avoid the detrimental heavy molybdenum sulfurization, responsible for the bad charge extraction. Finally, the deposition step could be improved further by complete automation, by upgrading the system to ink-jet printing of the precursor solution, in order to make the whole process human-variable-free and not waste raw materials.

AUTHOR INFORMATION

Corresponding Author

Simona O. Binetti − *Department of Materials Science and Solar Energy Research Center (MIB-SOLAR), University of Milano-Bicocca, 20125 Milano, Italy;* orcid.org/0000-0002-8605-3896; Email: simona.binetti@unimib.it

Authors

Giorgio Tseberlidis − *Department of Materials Science and Solar Energy Research Center (MIB-SOLAR), University of Milano-Bicocca, 20125 Milano, Italy;* orcid.org/0000-0002-9224-180X

Vanira Trifiletti − *Department of Materials Science and Solar Energy Research Center (MIB-SOLAR), University of Milano-Bicocca, 20125 Milano, Italy*

Elisa Vitiello − *Department of Materials Science and Solar Energy Research Center (MIB-SOLAR), University of Milano-Bicocca, 20125 Milano, Italy;* orcid.org/0000-0002-6952-2531

Amin Hasan Husien − *Department of Materials Science and Solar Energy Research Center (MIB-SOLAR), University of Milano-Bicocca, 20125 Milano, Italy*

Luigi Frioni − *Department of Materials Science and Solar Energy Research Center (MIB-SOLAR), University of Milano-Bicocca, 20125 Milano, Italy*

Mattia Da Lisca − *Institut Photovoltaïque d'Ile de France, 91120 Palaiseau, France; Université Paris-Saclay, CentraleSupélec, CNRS, Laboratoire de Génie Electrique et Electronique de Paris, 91192 Gif-sur-Yvette, France; Sorbonne Université CNRS, Laboratoire de Génie Electrique et Electronique de Paris, 75252 Paris, France*

José Alvarez − *Institut Photovoltaïque d'Ile de France, 91120 Palaiseau, France; Université Paris-Saclay, CentraleSupélec, CNRS, Laboratoire de Génie Electrique et Electronique de Paris, 91192 Gif-sur-Yvette, France; Sorbonne Université CNRS, Laboratoire de Génie Electrique et Electronique de Paris, 75252 Paris, France*

Maurizio Acciarri − *Department of Materials Science and Solar Energy Research Center (MIB-SOLAR), University of Milano-Bicocca, 20125 Milano, Italy*

Complete contact information is available at: https://pubs.acs.org/10.1021/acsomega.2c01786

Author Contributions

The manuscript was written through contributions of all authors. All authors have given approval to the final version of the manuscript.

Notes

The authors declare no competing financial interest.

ACKNOWLEDGMENTS

The authors acknowledge the project PON named "Bifacial Efficient Solar Cell Technology with 4-Terminal Architecture for Utility Scale" called "BEST-4U", financed by the Italian Ministry MIUR (CUPB88D19000160005). This work was also supported by the University of Milano-Bicocca through "Bando Infrastrutture di Ricerca 2021". Also, the Italian Ministry of University and Research (MIUR) through grant "Dipartimenti di Eccellenza-2017 Materials For Energy". The authors are grateful to Berenice Colombo (B.Sc.) for her precious help in the experimental procedures and technical operations carried out for this work.

REFERENCES

(1) Ito, K. *Copper Zinc Tin Sulfide-Based Thin Film Solar Cells*; Wiley Books, 2015.

(2) Le Donne, A.; Trifiletti, V.; Binetti, S. New Earth-Abundant Thin Film Solar Cells Based on Chalcogenides. *Front. Chem.* **2019**, *7*, 297.

(3) Su, Z.; Liang, G.; Fan, P.; Luo, J.; Zheng, Z.; Xie, Z.; Wang, W.; Chen, S.; Hu, J.; Wei, Y.; Yan, C.; Huang, J.; Hao, X.; Liu, F. Device Postannealing Enabling over 12% Efficient Solution-Processed Cu2ZnSnS4 Solar Cells with Cd2+ Substitution. *Adv. Mater.* **2020**, *32*, 2000121.

(4) Wang, W.; Winkler, M. T.; Gunawan, O.; Gokmen, T.; Todorov, T. K.; Zhu, Y.; Mitzi, D. B. Device Characteristics of CZTSSe Thin-Film Solar Cells with 12.6% Efficiency. *Adv. Energy Mater.* **2014**, *4*, 1301465.

(5) Kois, J.; Polivtseva, S.; Mamedov, D.; Samieipour, A.; Karazhanov, S. Z. Visible Light-Assisted Instability of Kesterite Cu2ZnSnS4: What Are the Implications? *Sol. Energy Mater. Sol. Cells* **2020**, *208*, 110384.

(6) Giraldo, S.; Jehl, Z.; Placidi, M.; Izquierdo-Roca, V.; Pérez-Rodríguez, A.; Saucedo, E. Progress and Perspectives of Thin Film Kesterite Photovoltaic Technology: A Critical Review. *Adv. Mater.* **2019**, *31*, 1806692.

(7) Liu, F.; Wu, S.; Zhang, Y.; Hao, X.; Ding, L. Advances in Kesterite Cu2ZnSn(S, Se)4 Solar Cells. *Sci. Bull.* **2020**, *65*, 698−701.

(8) Pal, K.; Singh, P.; Bhaduri, A.; Thapa, K. B. Current Challenges and Future Prospects for a Highly Efficient (>20%) Kesterite CZTS Solar Cell: A Review. *Sol. Energy Mater. Sol. Cells* **2019**, *196*, 138−156.

(9) Valentini, M.; Malerba, C.; Serenelli, L.; Izzi, M.; Salza, E.; Tucci, M.; Mittiga, A. Fabrication of Monolithic CZTS/Si Tandem Cells by Development of the Intermediate Connection. *Sol. Energy* **2019**, *190*, 414−419.

(10) Espindola-Rodriguez, M.; Sylla, D.; Sánchez, Y.; Oliva, F.; Grini, S.; Neuschitzer, M.; Vines, L.; Izquierdo-Roca, V.; Saucedo, E.; Placidi, M. Bifacial Kesterite Solar Cells on FTO Substrates. *ACS Sustainable Chem. Eng.* **2017**, *5*, 11516−11524.

(11) Tseberlidis, G.; Hasan Husien, A.; Riva, S.; Frioni, L.; Le Donne, A.; Acciarri, M.; Binetti, S. Semi-Transparent Cu2ZnSnS4

Solar Cells by Drop-Casting of Sol-Gel Ink. *Sol. Energy* **2021**, *224*, 134−141.
(12) Trifiletti, V.; Tseberlidis, G.; Colombo, M.; Spinardi, A.; Luong, S.; Danilson, M.; Grossberg, M.; Fenwick, O.; Binetti, S. Growth and Characterization of Cu2Zn1-XFexSnS4 Thin Films for Photovoltaic Applications. *Materials* **2020**, *13*, 1471.
(13) Le Donne, A.; Marchionna, S.; Acciarri, M.; Cernuschi, F.; Binetti, S. Relevant Efficiency Enhancement of Emerging Cu2MnSnS4 Thin Film Solar Cells by Low Temperature Annealing. *Sol. Energy* **2017**, *149*, 125−131.
(14) Rudisch, K.; Espinosa-García, W. F.; Osorio-Guillén, J. M.; Araujo, C. M.; Platzer-Björkman, C.; Scragg, J. J. S. Structural and Electronic Properties of Cu2MnSnS4 from Experiment and First-Principles Calculations. *Phys. Status Solidi* **2019**, *256*, 1800743.
(15) Beraich, M.; Taibi, M.; Guenbour, A.; Zarrouk, A.; Boudalia, M.; Bellaouchou, A.; Tabyaoui, M.; Mansouri, S.; Sekkat, Z.; Fahoume, M. Preparation and Characterization of Cu2CoSnS4 Thin Films for Solar Cells via Co-Electrodeposition Technique: Effect of Electrodeposition Time. *Optik* **2019**, *193*, 162996.
(16) Saha, A.; Figueroba, A.; Konstantatos, G. Ag2ZnSnS4 Nanocrystals Expand the Availability of RoHS Compliant Colloidal Quantum Dots. *Chem. Mater.* **2020**, *32*, 2148−2155.
(17) Lafond, A.; Guillot-Deudon, C.; Vidal, J.; Paris, M.; La, C.; Jobic, S. Substitution of Li for Cu in Cu2ZnSnS4: Toward Wide Band Gap Absorbers with Low Cation Disorder for Thin Film Solar Cells. *Inorg. Chem.* **2017**, *56*, 2712−2721.
(18) Li, F.; Xia, Z.; Liu, Q. Insight into the Controlled Synthesis of Cu2Zn(Ge,Sn)S4 Nanoparticles with Selective Grain Size. *J. Phys. Chem. C* **2016**, *120*, 16969−16976.
(19) Neuschitzer, M.; Marquez, J.; Giraldo, S.; Dimitrievska, M.; Placidi, M.; Forbes, I.; Izquierdo-Roca, V.; Pérez-Rodriguez, A.; Saucedo, E. Voc Boosting and Grain Growth Enhancing Ge-Doping Strategy for Cu2ZnSnSe4 Photovoltaic Absorbers. *J. Phys. Chem. C* **2016**, *120*, 9661−9670.
(20) Khadka, D. B.; Kim, S.; Kim, J. Effects of Ge Alloying on Device Characteristics of Kesterite-Based CZTSSe Thin Film Solar Cells. *J. Phys. Chem. C* **2016**, *120*, 4251−4258.
(21) Khadka, D. B.; Kim, J. Band Gap Engineering of Alloyed Cu2ZnGexSn1−XQ4 (Q = S,Se) Films for Solar Cell. *J. Phys. Chem. C* **2015**, *119*, 1706−1713.
(22) Ikeda, S.; Fujikawa, S.; Harada, T.; Nguyen, T. H.; Nakanishi, S.; Takayama, T.; Iwase, A.; Kudo, A. Photocathode Characteristics of a Spray-Deposited Cu2ZnGeS4 Thin Film for CO2 Reduction in a CO2-Saturated Aqueous Solution. *ACS Appl. Energy Mater.* **2019**, *2*, 6911−6918.
(23) Umehara, M.; Tajima, S.; Takeda, Y.; Motohiro, T. Wide Bandgap Cu2ZnSn1−xGexS4 Fabricated on Transparent Conductive Oxide-Coated Substrates for Top-Cells of Multi-Junction Solar Cells. *J. Alloys Compd.* **2016**, *689*, 713−717.
(24) Nwambaekwe, K. C.; John-Denk, V. S.; Douman, S. F.; Mathumba, P.; Yussuf, S. T.; Uhuo, O. V.; Ekwere, P. I.; Iwuoha, E. I. Crystal Engineering and Thin-Film Deposition Strategies towards Improving the Performance of Kesterite Photovoltaic Cell. *J. Mater. Res. Technol.* **2021**, *12*, 1252−1287.
(25) Tseberlidis, G.; Trifiletti, V.; Le Donne, A.; Frioni, L.; Acciarri, M.; Binetti, S. Kesterite Solar-Cells by Drop-Casting of Inorganic Sol−Gel Inks. *Sol. Energy* **2020**, *208*, 532−538.
(26) Trifiletti, V.; Mostoni, S.; Butrichi, F.; Acciarri, M.; Binetti, S.; Scotti, R. Study of Precursor-Inks Designed for High-Quality Cu 2 ZnSnS 4 Films for Low-Cost PV Application. *ChemistrySelect* **2019**, *4*, 4905−4912.
(27) Garcia-Llamas, E.; Guc, M.; Bodnar, I. V.; Fontané, X.; Caballero, R.; Merino, J. M.; León, M.; Izquierdo-Roca, V. Multiwavelength Excitation Raman Scattering of Cu2ZnSn1-XGex-(S,Se)4 Single Crystals for Earth Abundant Photovoltaic Applications. *J. Alloys Compd.* **2017**, *692*, 249−256.
(28) Sousa, M. G.; da Cunha, A. F.; Fernandes, P. A.; Teixeira, J. P.; Sousa, R. A.; Leitão, J. P. Effect of Rapid Thermal Processing Conditions on the Properties of Cu2ZnSnS4 Thin Films and Solar Cell Performance. *Sol. Energy Mater. Sol. Cells* **2014**, *126*, 101−106.
(29) Podsiadlo, S.; Bialoglowski, M.; Fadaghi, M.; Gebicki, W.; Jastrzebski, C.; Zero, E.; Trzybinski, D.; Wozniak, K. Synthesis of Magnetic Doped Kesterite Single Crystals. *Cryst. Res. Technol.* **2015**, *50*, 690−694.
(30) Chen, G.; Wang, W.; Chen, S.; Whang, Z.; Huang, Z.; Zhang, B.; Kong, X. Bandgap Engineering of Cu2ZnSn1-XGexS(e)4 by Adjusting Sn-Ge Ratios for Almost Full Solar Spectrum Absorption. *J. Alloys Compd.* **2017**, *718*, 236−245.
(31) Hamanaka, Y.; Matsumoto, K. Non-Vacuum Fabrication of Bandgap-Controlled CZTGS Alloy Films Using CZTS+CZGS Mixed Nanoparticle Inks. *Mater. Sci. Forum* **2021**, *1016*, 509−515.
(32) Engberg, S.; Canulescu, S.; Schou, J. Liquid Phase Assisted Grain Growth in Cu2ZnSnS4 Nanoparticle Thin Films by Alkali Element Incorporation. *RSC Adv.* **2018**, *8*, 7152−7158.
(33) Tauc, J.; Menth, A. States in the Gap. *J. Non-Cryst. Solids* **1972**, *8−10*, 569−585.
(34) Rajagopal, A.; Yang, Z.; Jo, S. B.; Braly, I. L.; Liang, P.-W.; Hillhouse, H. W.; Jen, A. K.-Y. Highly Efficient Perovskite−Perovskite Tandem Solar Cells Reaching 80% of the Theoretical Limit in Photovoltage. *Adv. Mater.* **2017**, *29*, 1702140.
(35) Eperon, G. E.; Leijtens, T.; Bush, K. A.; Prasanna, R.; Green, T.; Wang, J. T.-W.; McMeekin, D. P.; Volonakis, G.; Milot, R. L.; May, R.; Palmstrom, A.; Slotcavage, D. J.; Belisle, R. A.; Patel, J. B.; Parrott, E. S.; Sutton, R. J.; Ma, W.; Moghadam, F.; Conings, B.; Babayigit, A.; Boyen, H.-G.; Bent, S.; Giustino, F.; Herz, L. M.; Johnston, M. B.; McGehee, M. D.; Snaith, H. J. Perovskite-Perovskite Tandem Photovoltaics with Optimized Band Gaps. *Science* **2016**, *354*, 861−865.
(36) Zhao, D.; Wang, C.; Song, Z.; Yu, Y.; Chen, C.; Zhao, X.; Zhu, K.; Yan, Y. Four-Terminal All-Perovskite Tandem Solar Cells Achieving Power Conversion Efficiencies Exceeding 23%. *ACS Energy Lett.* **2018**, *3*, 305−306.
(37) Ferhati, H.; Djeffal, F.; Drissi, B. L. Performance Improvement of Perovskite/CZTS Tandem Solar Cell Using Low-Cost ZnS/Ag/ITO Multilayer Spectrum Splitter. *Superlattices Microstruct.* **2020**, *148*, 106727.
(38) Gershon, T.; Bishop, D.; Antunez, P.; Singh, S.; Brew, K. W.; Lee, Y. S.; Gunawan, O.; Gokmen, T.; Todorov, T.; Haight, R. Unconventional Kesterites: The Quest to Reduce Band Tailing in CZTSSe. *Curr. Opin. Green Sustainable Chem.* **2017**, *4*, 29−36.
(39) Lee, Y. S.; Gershon, T.; Gunawan, O.; Todorov, T. K.; Gokmen, T.; Virgus, Y.; Guha, S. Cu2ZnSnSe4 Thin-Film Solar Cells by Thermal Co-Evaporation with 11.6% Efficiency and Improved Minority Carrier Diffusion Length. *Adv. Energy Mater.* **2015**, *5*, 1401372.
(40) Van Puyvelde, L.; Lauwaert, J.; Pianezzi, F.; Nishiwaki, S.; Smet, P. F.; Poelman, D.; Tiwari, A. N.; Vrielinck, H. Influence of an Sb Doping Layer in CIGS Thin-Film Solar Cells: A Photoluminescence Study. *J. Phys. D: Appl. Phys.* **2013**, *47*, 45102.
(41) Enkhbat, T.; Mina, M. S.; Sharif, M. H.; Enkhbayar, E.; Jung, K. Y.; Shin, D. W.; Cho, S. W.; Jeon, C.-W.; Kim, J. Characteristic Material Parameters of CIGS Solar Cell Related with Device Performance. *Curr. Appl. Phys.* **2020**, *20*, 1237−1243.
(42) Oueslati, S.; Grossberg, M.; Kauk-Kuusik, M.; Mikli, V.; Ernits, K.; Meissner, D.; Krustok, J. Effect of Germanium Incorporation on the Properties of Kesterite Cu2ZnSn(S,Se)4 Monograins. *Thin Solid Films* **2019**, *669*, 315−320.
(43) Krustok, J.; Raadik, T.; Grossberg, M.; Kauk-Kuusik, M.; Trifiletti, V.; Binetti, S. Photoluminescence Study of Deep Donor-Deep Acceptor Pairs in Cu2ZnSnS4. *Mater. Sci. Semicond. Process.* **2018**, *80*, 52−55.
(44) Li, J.; Wang, H.; Luo, M.; Tang, J.; Chen, C.; Liu, W.; Liu, F.; Sun, Y.; Han, J.; Zhang, Y. 10% Efficiency Cu2ZnSn(S,Se)4 Thin Film Solar Cells Fabricated by Magnetron Sputtering with Enlarged Depletion Region Width. *Sol. Energy Mater. Sol. Cells* **2016**, *149*, 242−249.

https://doi.org/10.1021/acsomega.2c01786
ACS Omega 2022, 7, 23445−23456

(45) Zoppi, G.; Forbes, I.; Miles, R. W.; Dale, P. J.; Scragg, J. J.; Peter, L. M. Cu2ZnSnSe4 Thin Film Solar Cells Produced by Selenisation of Magnetron Sputtered Precursors. *Prog. Photovolt.: Res. Appl.* **2009**, *17*, 315−319.
(46) Sahu, M.; Minnam Reddy, V. R.; Park, C.; Sharma, P. Review Article on the Lattice Defect and Interface Loss Mechanisms in Kesterite Materials and Their Impact on Solar Cell Performance. *Sol. Energy* **2021**, *230*, 13−58.
(47) Heo, J.; Won, S. Scanning Probe Study on the Photovoltaic Characteristics of a Si Solar Cell by Using Kelvin Force Microscopy and Photoconductive Atomic Force Microscopy. *Thin Solid Films* **2013**, *546*, 353−357.
(48) Ma, Z.-M.; Mu, J.-L.; Tang, J.; Xue, H.; Zhang, H.; Xue, C.-Y.; Liu, J.; Li, Y.-J. Potential Sensitivities in Frequency Modulation and Heterodyne Amplitude Modulation Kelvin Probe Force Microscopes. *Nanoscale Res. Lett.* **2013**, *8*, 532.
(49) Melitz, W.; Shen, J.; Kummel, A. C.; Lee, S. Kelvin Probe Force Microscopy and Its Application. *Surf. Sci. Rep.* **2011**, *66*, 1−27.

https://doi.org/10.1021/acsomega.2c01786
ACS Omega 2022, 7, 23445−23456